

Understanding fine structure of latent track in rutile TiO₂

Pengfei Zhai^{1,*}, Shuai Nan^{2,3}, Lijun Xu^{1,3}, Weixing Li², Zongzhen Li^{1,3}, Peipei Hu^{1,3}, Jian Zeng¹, Shengxia Zhang¹, Youmei Sun¹ & Jie Liu^{1,†}

¹ *Institute of Modern Physics, Chinese Academy of Sciences, Lanzhou 730000, China*

² *CAS Center for Excellence in Tibetan Plateau Earth Sciences, and Key Laboratory of Continental Collision and Plateau Uplift, Institute of Tibetan Plateau Research, Chinese Academy of Sciences, Beijing 100101, China*

³ *University of Chinese Academy of Sciences, Beijing 100049, China*

Understanding the formation of latent track by energetic heavy ions is important for the fields of nuclear waste disposal, nuclear fuel and modification of materials.

However, the details of the mechanism for the track formation in non-amorphizable materials are still being debated. Here, we report on the fine structure formation of latent tracks, which changes from cylinder to sandglass as a function of the ion-penetrating length, in a typical non-amorphizable material, rutile TiO₂. Based on inelastic thermal spike model, we show that the outflow of molten phase produces the hillocks on surface and the void-rich zone near surface, while at a deep depth, the lack of outflow and the rapid recrystallization result in the absence of tracks. Moreover, the morphology of tracks depends on the velocity of molten phase outflow and recrystallization. Our perspective provides a new interpretation in the radiation damage for both amorphizable and non-amorphizable materials.

* Corresponding author. E-mail address: zhaipengfei@impcas.ac.cn (P. Zhai)

† Corresponding author. E-mail address: j.liu@impcas.ac.cn (J. Liu)

Rutile (TiO_2) polymorphs have widespread applications in solar cell^{1,2}, photocatalyst³⁻⁵, single-phase ceramic nuclear waste form^{6,7} and high dielectric gate insulator for the new generation of metal-oxide-semiconductor field-effect transistor (MOSFET)⁸. Ion irradiations in rutile are of importance because the physical, electronic and photocatalytic performance in TiO_2 can be significantly improved⁹⁻¹⁵. As an example, ion implantation has been demonstrated to shift the absorption band to the visible light region in TiO_2 ⁹⁻¹³, whereas the wide bandgap in the conventional TiO_2 results in only about 3-5% of the total solar light for energy conversion. However, the failure of material used in nuclear waste form induced by fission fragment^{6,7} or breakdown of gate oxide in MOSFET caused by space irradiation¹⁶ is harmful to the service life. Therefore, it is a long-standing objective in material science to understand the correlation between intrinsic properties and its behavior to energetic heavy ions.

In material irradiation society, insulator materials were simply classified into amorphizable materials and non-amorphizable materials, judging from the nature of ion track as amorphous or not. In this way, the insulator materials such as CaF_2 ^{17,18}, UO_2 ^{19,20}, CeO_2 ^{21,22}, TiO_2 ^{23,24}, yttria-stabilized cubic ZrO_2 (YSZ)^{25,26}, $\text{Gd}_2\text{Zr}_2\text{O}_7$ ²⁷ and apatite²⁸ are non-amorphizable materials. This is because their internal structure within an ion track is porous, or not amorphous, which is different from the amorphous tracks in amorphizable materials²⁹. For amorphizable materials, the experimental track data usually coincide quite well with the calculations of the widely used inelastic thermal spike model (i-TS model)³⁰⁻³⁴, when the melting criterion is used. However, for non-amorphizable materials, the experimental diameters of ion

track as obtained by transmission electron microscopy (TEM) are much smaller than the i-TS model calculations, if the melting criterion for track formation is still applied^{25,26,35}. The i-TS model calculations are found to coincide with the TEM data in ion-irradiated CaF₂ when a boiling criterion replaces the melting one³⁵. However, the use of boiling criterion is not supported by a recent TEM result that very low threshold (3 keV/nm) for track formation is found in 10-23 MeV I ion irradiated CaF₂¹⁸, because the electronic energy loss is not high enough to raise the track core to boiling temperature.

As a typical non-amorphizable material, rutile irradiated by swift heavy ions has been investigated intensely by TEM^{23,24,36}, atomic force microscopy (AFM)³⁷⁻⁴¹, Rutherford backscattering in channeling mode (RBS/C)⁴⁰, and grazing-incidence small-angle X-ray scattering (GISAXS)⁴¹. Hillocks on the surface of specimen, after bombarded with swift heavy ions under normal or grazing incidence angle, were observed by AFM and scanning electron microscopy³⁷⁻⁴¹. More recently, the conical tracks consist of an agglomeration of 1–2 nm sized features near surface of rutile, was observed by TEM^{23,24}. As the detailed morphology and structure of irradiation-induced damage along the entire length of ion tracks has not been revealed, the reduced internal pressure near surface of rutile has been considered responsible for the formation of conical morphology of ion track²⁴.

In this study, by controlling the incident angle, we are able to observe the morphological change at each place along the entire length of an ion track in ion-irradiated rutile, which consists of a pair of hillocks on surfaces, a conical and

porous ion track beneath the hillocks, and undamaged regime below the tracks. This full picture of the ion track allows us to systematically investigate the formation and structure of both damaged and undamaged regimes. Based on i-TS model, we give a new insight into the ion track formation for both amorphizable and non-amorphizable materials.

Results

Track morphology as a function of ion path length

Bright field TEM images show the ion tracks in lamella rutile induced by 1390 MeV Bi ions (Fig. 1). An individual ion track appears as nearly cylindrical and continuous. It consists of irregular structures (Fig. 1a), which have white core and dark fringe at under focus condition, dark core and white fringe at over focus condition, and little contrast at focus condition. This can be understood by Fresnel contrast, a typical TEM technique to view cavities or highly porous tracks^{17,21,23,28,42,43}. At both ends of an ion track, circular features, which were assigned as spherical hillocks formation at the entrance and exit surfaces of ion trajectory^{17,21,43}, are also visible. It was reported that the hillocks of irradiated rutile TiO₂ are crystalline²¹, just like the hillocks of irradiated CeO₂²¹, because the lattice spacing and orientation of the hillocks coincide with those of the matrix. In this study, the average size of the hillocks (10.2 ± 1.6 nm) is slightly larger than that of the corresponding track (8.4 ± 1.6 nm). Note that several small isolated islands are visible (Fig. 1a), with an average diameter of the isolated islands about half of the hillocks. The inhomogeneous contrast inside the tracks can be identified clearly by HRTEM (Fig. 1b). Except a few

faceted structures, the voids appear almost irregular, significantly different from the well aligned, faceted anion voids, which are a sign of preferential creation voids along specific directions, in irradiated CaF_2 ¹⁷.

In Fig. 1c, the entire length of a sandglass-like structure in irradiated lamella rutile with Bi ions is visible by TEM under overfocused condition. The “waist” of the sandglass is marked by arrows. This sandglass-like morphology is different from the cylindrical morphology shown in Fig. 1a. It is not due to the reducing of electronic energy loss of 1390 MeV Bi ions in lamella rutile, because the electronic energy loss is almost unchanged (39.9 keV/nm) for such a short depth change in this thin sample. Moreover, the narrow part is just in the middle of the tracks. We interpret this discrepancy in terms of the difference of ion path length. Note that the real ion path length of the two tracks in Fig. 1c is longer.

Our assumption that track morphologies are different for different ion path lengths is further confirmed, as an example is shown in Fig. 1d. In the bottom right corner, the morphology of the track (marked by 1) is similar to that of the tracks in Fig. 1c. It is interesting to note that in Fig. 1d, different track morphology can be seen in other locations as labeled by 2 and 3. For each track, there is always a pair of two hillocks on bottom and top surfaces, connecting a narrowing track near surface. However, as the track diameter decrease, the track appears as a continuous line at a shallow depth (as in 2), or as a discontinuous line (as in 3) at a deeper depth.

In Fig. 2, a sketch is used in order to systematically describe the four different morphologies of ion track in rutile as a function of ion path length, based on our TEM

observations.

Hillocks on surfaces

The topographies of the irradiated rutile surface were observed by AFM (Fig. 3). The hillocks induced by 1390 MeV Bi ions at a fluence of $5 \times 10^{11} \text{ cm}^{-2}$ appear almost overlapped (Fig. 3a). However, the estimated ratio of ion affected region should be only 39%, considering the diameter of the individual hillock being $\sim 10 \text{ nm}$ (Fig. 1). It is because the finite curvature radius of the tip (nominally 10 nm for Arrow-UHF tip) induces the notable broadening effect for the hillocks in lateral direction. However, the resolution in vertical direction is mainly affected by the noise of the Z sensor of AFM ($<50 \text{ pm}$ in closed loop condition for Cypher) instead of the finite curvature radius of the tip. Moreover, the hillock height determined by AFM has been considered as an appropriate parameter to describe the behavior of ion track formation versus the electronic energy loss in $\text{Y}_3\text{Fe}_5\text{O}_{12}$ (YIG)⁴⁴. By assuming that the spherical hillocks exactly protrude out of the specimen surface, as in the cases of the irradiated CeO_2 ²¹, we carefully used the average hillock height to represent the diameter of track, despite that the track diameter is slightly smaller than the spherical diameter of hillock (Fig. 1). These hillock yields (η , hillock number/ion fluence) and heights (D_h) with standard deviation induced by Xe and Ta ions were analyzed using built-in analysis software through Gaussian fitting to the center heights of the hillocks. Considering the experimental errors (10-20%) in the ion fluence, one can conclude that an incident ion almost creates one hillock as the calculated hillock yield is about 80-100%. The heights of the hillocks are presented in Table 1.

Alternatively, all of the corrected diameters of hillocks can be also obtained (Table 1) using a simple deconvolution approach $D_c = D_a^2/4D_t^{46}$, where D_c is the corrected diameters of hillocks, D_a is the apparent diameter of hillocks and D_t is the tip diameter (20 nm). These corrected diameters are actually very close to the heights of hillocks (Table 1). It confirms that the hillocks are spherical and the whole sphere almost reaches out of the surface.

i-TS model calculations versus experimental results

Using the thermal spike model, Awazu et al.³⁶ calculated the ion track size directly from the radius of lattice temperature over the equilibrium melting point T_m of rutile (2130 K). However, the latent heat of fusion (838.07 kJ/g⁴⁷), which is crucial for the transition of rutile from solid to liquid, was not considered. Furthermore, due to the transient and huge heating rate of the atoms, T_m is actually not the adequate parameter to characterize the melting process, as experimentally proven by femtosecond laser experiments^{48,49}. As was also suggested by Rethfeld et al.⁵⁰, the temperature that allows for homogeneous nucleation of a liquid phase induced by ultra-short pulsed laser irradiation should be $\sim 1.4T_m$ within a few picoseconds. Thus, without considering superheating, one probably underestimates the electronic energy loss threshold of track formation in rutile, and in turn overestimates the size of ion tracks under high electronic excitation^{30,32}.

Other than the boiling criterion, we assume that the melting criterion is associated with the ion track formation in irradiated rutile. The calculated results by i-TS model for 1390 MeV Bi irradiation are displayed in Fig 4. Within superheating scenario, the

energy to melt E_m has been considered as the criterion for the transition from solid to liquid phase^{30,32,35}. For rutile, the energy to reach the melting point is 0.46 eV/at (initial temperature 300 K), while the solid to liquid phase transition energy (latent heat of fusion) is 0.23 eV/at⁴⁷. Thus, the corresponding radius 4.3 nm can be determined by $E_m = 0.69$ eV/at (Fig. 4a). It must be emphasized that i-TS model just gives a prediction for initial track size without considering a recrystallization process. One can notice that the lifetime of molten TiO_2 for different radial distances from the core is different (Fig. 4a), for instance, the duration of molten phase for radius of 0.5 and 4.3 nm are about $t_{0.5}=11.1$ ps and $t_{4.3}=1.5$ ps, respectively. This core-shell distribution due to different duration of melted phase will be used to explain the formation of conical feature of ion track. The superheating atomic temperature versus time is also given in Fig. 4b. For the radius of 4.3 nm, superheating melting temperature T_S is determined as 2900 K with the heating rate $\sim 10^{15}$ K/s. The calculated T_S is larger than the equilibrium melting point (2130 K) by a factor of 1.36, consistent with the calculated result by Rethfeld et al.⁵⁰, where transient thermal melting was considered as homogeneous nucleation of the liquid phase in a femtosecond laser-excited bulk.

The experimental radii from previous work^{23,36,40,51,52} and the present work are compared with i-TS calculations within superheating scenario (Fig. 5). It indicates that most of experimental data agree quite well with i-TS model calculations, with one exception, as marked with the open pink circle reproduced from Awazu et al.³⁶. For example, the track radius induced by 115 MeV Br (16.1 keV/nm) is ~ 2.6 times higher

than the prediction of i-TS model. The discrepancy is possibly because the authors considered the etched track as latent ion track. However, after 20% HF etching for 10s, both the stressed part and the amorphous core were etched. According to the Fig. 1(c) from Ref. 36, the unetched track radius induced by 115 MeV Br is only about 1.0 nm, evidently smaller than the reported size of 3.7 nm after etching. Note that in another paper by Awazu et al.⁵¹, the radius of unetched track induced by 84.5 MeV Cu ions (13.6 keV/nm) is 0.9 ± 0.2 nm, which is consistent well with our i-TS prediction (open red circle). It was reported that after a high fluence ($>6 \times 10^{12}$ ions/cm²) of 167 MeV Xe irradiation, the rutile crystal is amorphized, extending from the surface down to 8.3 μm below, where the remaining energy is about 15 MeV with a corresponding electronic stopping power ~ 7.3 keV/nm²³. This value coincides well with the present i-TS prediction for 0.1 MeV u⁻¹ ion irradiation (Fig. 5), indicating that the threshold for electronic energy loss is ~ 7 keV/nm.

Electronic energy loss threshold predicted by i-TS model

Electronic energy loss threshold $(dE/dx)_{\text{th}}$ for ion track formation in single crystal rutile as predicted by i-TS model is plotted as a function of beam energy ranging from 0.1 to 100 MeV/u (Fig. 6). This range basically covers the ability of international large heavy ion accelerator facilities, including HIRFL (China), UNILAC (Germany) and GANIL (France). It is shown that $(dE/dx)_{\text{th}}$ ranges from 7 to 24 keV/nm as a function of beam energy. The significantly increased threshold values as the beam energy increases can be explained by the well-established ion velocity effect^{32,33,53}, which has been taken into account in i-TS model in the term of $A(r[v], t)$ (see

“Inelastic thermal spike model” in Methods). Besides that $(dE/dx)_{th}$ for 0.1 MeV/u is consistent with the experimental result²³, it also agrees with the experimental estimation of 8.9-10.4 keV/nm by Karlusic et al.⁴⁰, where 23 and 28 MeV I ions were used, corresponding to the calculated $(dE/dx)_{th}$ 8.5 keV/nm for 0.2 MeV/u.

Discussion

Why is the deduced track size by RBS/C close to the i-TS model prediction?

As observed by TEM, the morphology of ion track near the surface of rutile (~60 nm²³) is conical and the track radius in the deep is much thinner (~1 nm as shown in Fig. 1d). Logically, the effective radius deduced from RBS/C, which assumes that the tracks have identical size and cylindrical symmetry⁴⁰, is expected to be much smaller than our calculation by i-TS model. However, it is interesting that the deduced track size from RBS/C⁴⁰ agrees well with the present i-TS model prediction (Fig. 5).

We suggest that it is the strained region^{36,51} and/or the defective channel around the track^{54,55}, which the RBS/C measurement is also sensitive to within its detection depth, attribute to the additional backscattering yield. Although RBS/C cannot obtain the real track size or final track size, if knowing that the timescale of track formation is usually several picoseconds, it gives the estimation of initial track size for the irradiated rutile with swift heavy ions.

What are responsible for sandglass morphology of ion tracks?

A reduced internal pressure near surface of rutile has been suggested to be responsible for the formation of conical morphology of ion track²⁴. However, this model cannot explain why track morphology changes from an cylinder to a cone as a

function of ion path length in the same thickness of thin sample as shown in Fig. 2a,b. More importantly, as the authors point out, if the reduced internal pressure is true, these near surface conical features should be a general phenomenon. However, the ion tracks near surface in apatite⁵⁶, YIG^{29,57} and Gd₂TiO₇⁵⁸ are clearly cylindrical. As a fact, this phenomenon was observed undoubtedly only in rutile, YSZ and Al₂O₃ single crystal so far²³⁻²⁶. Similar to the above materials, CeO₂ can be another candidate having conical track near surface^{21,24}, as they are all defined as non-amorphizable materials (or “resistant materials” in some literature)^{30,59,60}.

We suggest that the near surface conical feature with small voids is not a general phenomenon, but limited to one kind of non-amorphizable materials that have a strong ability to recrystallize according to the original structure^{59,60}, and the molten phases have low viscosity and low density. The latter two enable the molten material near surface flow outwards moderately and cause partial mass deficiency for the voids formation in the track. Specifically, this near surface conical feature can be attributed to the competition of rapid fluid velocity and high recrystallization velocity during several picoseconds quenching. The specific lifetime of molten region induced by swift heavy ions is scaled with its radial distance from the core, i.e. the closer to the core, the longer lifetime of molten phase (Fig. 4). The track size and cylindrical morphology in rutile calculated by i-TS model can be regarded as the initial track size and shape.

In the case of irradiated rutile by 1390 MeV Bi ions, the calculated radius of initial track R_0 is 4.3 nm, which is the same size as that of surface track obtained by TEM as

shown in Fig. 1, while the radius of thin track connecting two conical parts is about 1.0 nm. We suggest that this thin track is formed as a result that the initial molten region around the track has been recrystallized, because the matter here has not flowed outwards yet. The lifetime of molten phase in the core t_{core} is 11.1 ps (Fig. 4a). Thus, the recrystallization velocity can be estimated as $v_{Re} = (4.3-1.0)/11.1 = 0.30$ nm/ps. The fluid velocity v_f can be estimated from the equation (1) - (4), assuming the spherical hillock formed due to the molten TiO_2 expelled from the initial track near surface:

$$V_f \cdot \rho_l = V_h \cdot \rho_s \quad (1)$$

$$V_h = \frac{4}{3} \pi R_h^3 \quad (2)$$

$$V_f = \int_0^{R_0} 2\pi r v_f \cdot t(r) dr \quad (3)$$

$$t(r) = 10.02 + 0.01r + 0.11r^2 - 0.13r^3 \quad (4)$$

where, V_f and V_h are the volume of molten TiO_2 flowing onto the surface and that of crystalline hillock, respectively, ρ_l is density of molten TiO_2 (3.21 g/cm^3), ρ_s is density of crystalline rutile (4.25 g/cm^3) and R_h is the radius of hillock (5.1 nm). Duration of molten phase $t(r)$ is a function of radial distance r from the core of thermal spike, which can be fitted by the i-TS calculation. Combining the equation (1) - (4), we get the v_f as 1.82 nm/ps. It should be emphasized that this fluid velocity is just the mean value for the whole molten region and duration of molten phase, as the fluid velocity is assumed to be constant in the above calculation.

However, the fluid velocity should be a function of the radial distance from the core and the thermal spike evolution time. As a first approximation, we use the

equation (5) instead of the constant v_f . The fluid velocity is a linear function of radial distance from the core, and can be assumed to be 5.4 nm/ps for the core region by considering that the duration of molten phase in core is 11.1 ps and the cone length is about 60 nm²³.

$$v_f(r) = 5.4 - 1.25r \quad (5)$$

Combining the equation (3)-(5), the volume of molten TiO₂ flowing onto the surface V_f can be obtained as 860.9 nm³. The difference between calculated value of mass deficit due to outflow and estimation from spherical hillock $(V_f \cdot \rho_l - V_h \cdot \rho_s) / V_h \cdot \rho_s$ is only about 17%. This confirms that the spherical hillock originates from the outflow of the molten TiO₂ in the initial thermal spike region, i.e., the mass deficit due to outflow near surface is responsible for voids formation after recrystallization.

It can be inferred that the mass deficit is ~15% (i.e., $\frac{4}{3}\pi R_h^3 \cdot \rho_s / \pi R_0^2 \cdot L \cdot \rho_s$, where L is 60 nm for the case of irradiated rutile by 1390 MeV Bi ion) for each end of track, in contrast to the case of ion-irradiated NiO, wherein the mass deficit is much higher (~100%) to form cylindrical nanotube⁴³. It further confirms that the proportion of mass deficit is dependent on fluid velocity, recrystallization velocity, and the viscosity and density of the molten phase.

Thus, different track morphologies can be obtained by changing the ion path length based on the experimental observations (refer to Fig. 1 and Fig. 2) and the thermal spike model analysis. This because that the velocity of fluid is much higher than that of recrystallization, which occurs at the interface between solid and liquid phase, and because the lifetime for molten phase is related to radial distance from the

core of thermal spike. When the ion path length is long enough (>60 nm), the conical morphology near surface appears (Fig. 1c). Especially, when the ion path length is about 150 nm, the sandglass ion track as shown in Fig. 1d appears. Oppositely, when the ion path length is very short (≤ 60 nm), the nearly cylindrical morphology appears (Fig. 1b). For the bulk rutile, the lack of enough outflow of molten material and rapid recrystallization result in no visible tracks at a deep depth.

Other phenomena in irradiated rutile may be explained based on the above argument: (1) The radius of the thin track connected with two conical parts of track is about 1 nm (Fig. 1d). It coincides with the radius of core of thermal spike, wherein the duration of molten phase is the longest (Fig. 4a). (2) The deduced radius by RBS/C is strikingly close to the calculated track size, i.e. the initial track size before recrystallization, by i-TS model, as shown in Fig. 5. The recrystallized region from the initial track, which acts as defective channels around the final track, probably contributes to the backscattering yield for the RBS/C measurement.

More interestingly, this model is applicable for both amorphizable and non-amorphizable materials irradiated by energetic heavy ions. For an amorphizable material, recrystallization is negligible. Consequently, the final track is amorphized with cylindrical shape. For a non-amorphizable material, the sandglass-like track is formed as a result of the competition between recrystallization and outflow of the molten material. The fluid velocity is scaled with the core-shell structure of thermal spike. Therefore, the specific angle and length of the cone depend on material and electronic energy loss. Especially, if the fluid velocity of molten material is large

enough, the final track is cylindrical nanotube just like the case of ion-irradiated NiO⁴³.

Methods

Swift heavy ion irradiation

Single crystals of rutile TiO₂ with sample size 10 × 10 × 0.5 mm³ and two different orientations of (110) and (001) were purchased from KJ-MTI Corporation, China. Surfaces were epi-polished down to root mean square (RMS) roughness ≤ 0.2 nm and the crystal miscut angle is less than 0.5°. The lamella samples were prepared by crushing in a mortar, mixing with ethanol, and depositing on a copper TEM grid covered with an amorphous carbon thin film.

The samples were irradiated with initial kinetic energy of 19.5 MeV/u ¹²⁹Xe at a fluence of 5 × 10¹⁰/cm² for normal incidence, 2 × 10¹⁰/cm² for 45° incidence, 12.5 MeV/u ¹⁸¹Ta at 1 × 10¹⁰/cm² for 7° incidence with respect to the normal of surface, and 9.5 MeV/u ²⁰⁹Bi at 5 × 10¹¹/cm² for normal incidence at Heavy Ion Research Facility in Lanzhou (HIRFL) at room temperature. The ion flux detected on-line by a detector with three aluminum foils (total thickness 18 μm) was less than 2 × 10⁸/cm²·s to avoid macroscopic sample heating. The fluence was determined with an estimated uncertainty of 10-20%. Aluminum degraders (99.99% purity) of different thicknesses were usually placed in front of the samples in order to change the energy. The detailed irradiation parameters are listed in Table 1. The calculated ion range in bulk samples is around 30-100 μm. However, by changing incidence angle and sample thickness, the actual penetrating length in a lamella sample was controlled to a range around

50-150 nm, which enables us to systematically investigate the change in track morphology as a function of ion length.

AFM and TEM characterization

To investigate the topography of the surface after irradiation, tapping mode AFM was performed using Cypher (Asylum Research, USA) at ambient atmosphere and Arrow-UHF (NanoWorld, Switzerland) with cantilever resonance frequencies of about 1.4 MHz. The images were analyzed using the built-in analysis software. The irradiated lamella samples were observed using a Tecnai G2 F20 S-TWIN TEM (FEI, USA) operating at 200 kV.

Inelastic thermal spike model

Based on the inelastic thermal spike (i-TS) model^{30,32,34}, two classical heat diffusion equations can be used to calculate the energy exchange between the electronic subsystem and atomic subsystem, driven by the temperature difference ($T_e - T_a$) between the electronic subsystem temperature (T_e) and atomic subsystem temperature (T_a), which is stimulated by the energy inputs into the electronic subsystem $A(r[v], t)$ from the electronic stopping powers for specific ion velocity v :

$$\begin{aligned} C_e(T_e) \frac{\partial T_e}{\partial t} &= \frac{1}{r} \frac{\partial}{\partial r} \left[r K_e(T_e) \frac{\partial T_e}{\partial r} \right] - g(T_e - T_a) + A(r[v], t) \\ C_a(T_a) \frac{\partial T_a}{\partial t} &= \frac{1}{r} \frac{\partial}{\partial r} \left[r K_a(T_a) \frac{\partial T_a}{\partial r} \right] + g(T_e - T_a) \end{aligned}$$

where C_e , C_a , K_e and K_a are the specific heats and thermal conductivities of the electronic and atomic subsystems, respectively. The electron-phonon coupling strength g is linked to the electron-phonon mean free path λ by the relation $\lambda \sim K_e/g^2$, which approximately equals B/g^2 (with $B= 2$ J/s/cm/K) in insulators^{32,34}, and is scaled

with the band gap E_g as determined by experimental results^{32-34,61}. Another key parameter in this model, the energy to melt E_m ^{32-34,61}, is 0.69 eV/at for rutile⁴⁷. The detailed physical properties of rutile TiO_2 used for the i-TS model calculation are presented in Table 2.

References

1. O'Regan, B. & Grätzel, M. A low-cost, high-efficiency solar cell based on dye-sensitized colloidal TiO_2 films. *Nature* **353**, 737-740 (1991).
2. Park, N.-G., van de Lagemaat, J. & Frank, A. J. Comparison of dye-sensitized rutile- and anatase-based TiO_2 solar cells. *J. Phys. Chem. B* **104**, 8989-8994 (2000).
3. Fujishima, A & Honda, K. Electrochemical photolysis of water at a semiconductor electrode. *Nature* **238**, 37-38 (1972).
4. Asahi, R., Morikawa, T., Ohwaki, T., Aoki, K. & Taga, Y. Visible-light photocatalysis in nitrogen-doped titanium oxides. *Science* **293**, 269-271 (2001).
5. Tao, J., Luttrell, T. & Batzill, M. A two-dimensional phase of TiO_2 with a reduced bandgap. *Nature Chem.* **3**, 296-300 (2011).
6. Weber, W. J. et al. Radiation effects in crystalline ceramics for the immobilization of high-level nuclear waste and plutonium. *J. Mater. Res.* **13**, 1434-1484 (1998).
7. Lumpkin, G. R. et al. Experimental and atomistic modeling study of ion irradiation damage in thin crystals of the TiO_2 polymorphs. *Phys. Rev. B* **77**, 214201 (2008).
8. Wilk, G. D., Wallace, R. M. & Anthony, J. M. High- κ gate dielectrics: Current status and materials properties considerations. *J. Appl. Phys.* **89**, 5243 (2001).
9. Anpo, M. Photocatalysis on titanium oxide catalysts: Approaches in achieving highly efficient reactions and realizing the use of visible light. *Catal. Surv. Asia* **1**, 169-179 (1997).
10. Yamashita, H., Ichihashi, Y., Takeuchi, M., Kishiguchi, S. & Anpo M. Characterization of metal ion-implanted titanium oxide photocatalysts operating under visible light irradiation. *J. Synchrotron Rad.* **6**, 451-452 (1999).
11. Shen, H., Mi, L., Xu, P., Shen W. & Wang, P. N. Visible-light photocatalysis of

- nitrogen-doped TiO₂ nanoparticulate films prepared by low-energy ion implantation. *Appl. Surf. Sci.* **253**, 7024-7028 (2007).
12. Yamashita, H. et al. Degradation of propanol diluted in water under visible light irradiation using metal ion-implanted titanium dioxide photocatalysts. *J. Photochem. Photobiol. A* **148**, 257-261 (2002).
13. Pelaez, M. et al. A review on the visible light active titanium dioxide photocatalysts for environmental applications. *Appl. Catal. B: Environ.* **125**, 331-349 (2012).
14. Meldrum, A., Jr. Haglund, R. F., Boatner, L. A. & White, C. W. Nanocomposite materials formed by ion implantation. *Adv. Mater.* **13**, 1431-1444 (2001).
15. Jain, I. P. & Agarwal, G. Ion beam induced surface and interface engineering. *Surf. Sci. Rep.* **66**, 77-172 (2011).
16. Massengill, L. W. et al. Heavy-ion-induced breakdown in ultra-thin gate oxides and high-k dielectrics. *IEEE Trans. Nucl. Sci.* **48**, 1904-1912 (2001).
17. Jensen, J., Dunlop, A. & Della-Negra, S. Microscopic observations of metallic inclusions generated along the path of MeV clusters in CaF₂. *Nucl. Instrum. Methods Phys. Res., Sect. B* **146**, 399-404 (1998).
18. Karlušić, M. et al. On the threshold for ion track formation in CaF₂. *New J. Phys.* **19**, 023023 (2017).
19. Sonoda, T. et al. Clarification of high density electronic excitation effects on the microstructure evolution in UO₂. *Nucl. Instrum. Methods Phys. Res., Sect. B* **268**, 3277-3281 (2010).
20. Ishikawa, N., Sonoda, T., Sawabe, T., Sugai, H. & Sataka, M. Electronic stopping power dependence of ion-track size in UO₂ irradiated with heavy ions in the energy range of ~1 MeV/u. *Nucl. Instrum. Methods Phys. Res., Sect. B* **314**, 180-184 (2013).
21. Ishikawa, N., Okubo, N. & Taguchi, T. Experimental evidence of crystalline hillocks created by irradiation of CeO₂ with swift heavy ions: TEM study. *Nanotechnology* **26**, 355701 (2015).
22. Takaki, S., Yasuda, K., Yamamoto, T., Matsumura, S. & Ishikawa, N. Structure of ion tracks in ceria irradiated with high energy xenon ions. *Prog. Nucl. Energy* **92**,

306-312 (2016).

23. O'Connell, J. H., Skuratov, V. A., Akilbekov, A., Zhumazhanova, A. & van Vuuren, A. J. EM study of latent track morphology in TiO₂ single crystals. *Nucl. Instrum. Methods Phys. Res., Sect. B* **379**, 200-205 (2016).
24. O'Connell, J., Skuratov, V., van Vuuren, A. J., Saifulin, M. & Akilbekov, A. Near surface latent track morphology of SHI irradiated TiO₂. *Phys. Status Solidi b* **253**, 2144-2149 (2016).
25. Moll, M. et al. Damage induced by electronic excitation in ion-irradiated yttria-stabilized zirconia. *J. Appl. Phys.* **105**, 023512 (2009).
26. Garrido, F., Moll, S., Sattonnay, G., Thom é L. & Vincent, L. Radiation tolerance of fluorite-structured oxides subjected to swift heavy ion irradiation. *Nucl. Instrum. Methods Phys. Res., Sect. B* **267**, 1451-1455 (2009).
27. Lang, M. et al. Swift heavy ion track formation in Gd₂Zr_{2-x}Ti_xO₇ pyrochlore: Effect of electronic energy loss. *Nucl. Instr. Methods Phys. Res. Sect. B* **336**, 102-115 (2014).
28. Li, W. et al. Porous fission fragment tracks in fluorapatite. *Phys. Rev. B* **82**, 144109 (2010).
29. Ishikawa, N., Taguchi, T. & Okubo, N. Hillocks created for amorphizable and non-amorphizable ceramics irradiated with swift heavy ions: TEM study. *Nanotechnology* **28**, 445708 (2017).
30. Toulemonde, M., Assmann, W., Dufour, C., Meftah, A. & Trautmann, C. Nanometric transformation of the matter by short and intense electronic excitation: Experimental data versus inelastic thermal spike model, *Nucl. Instr. Methods Phys. Res. Sect. B* **277**, 28-39 (2012).
31. Toulemonde, M., Trautmann, C., Balanzat, E., Hjort, K. & Weidinger, A. Track formation and fabrication of nanostructures with MeV-ion beams. *Nucl. Instr. Methods Phys. Res. Sect. B* **216**, 1-8 (2004).
32. Dufour, C. & Toulemonde, M. Models for description of track formation, in: W. Wesch, E. Wendler (Eds.), *Ion Beam Modification of Solids* (Springer International Publishing, Switzerland, 2016, pp. 63-104).

33. Meftah, A. et al. Experimental determination of track cross-section in $\text{Gd}_3\text{Ga}_5\text{O}_{12}$ and comparison to the inelastic thermal spike model applied to several materials. *Nucl. Instrum. Methods Phys. Res., Sect. B* **237**, 563-574 (2005).
34. Toulemonde, M., Dufour, C., Meftah, A. & Paumier, E. Transient thermal processes in heavy ion irradiation of crystalline inorganic insulators. *Nucl. Instrum. Methods Phys. Res., Sect. B* **166-167**, 903-912 (2000).
35. Toulemonde, M. et al. Dense and nanometric electronic excitations induced by swift heavy ions in an ionic CaF_2 crystal: Evidence for two thresholds of damage creation. *Phys. Rev. B* **85**, 054112 (2012).
36. Awazu, K. et al. Structure of latent tracks in rutile single crystal of titanium dioxide induced by swift heavy ions. *J. Appl. Phys.* **100**, 044308 (2006).
37. Akc ̇ltekin, E. et al. Creation of multiple nanodots by single ions. *Nature Nanotech.* **2**, 290-294 (2007).
38. Popok, V. N., Jensen, J., Vučković, S., Mackova, A. & Trautmann, C. Formation of surface nanostructures on rutile (TiO_2): comparative study of low-energy cluster ion and high-energy monoatomic ion impact. *J. Phys. D: Appl. Phys.* **42**, 205303 (2009).
39. Akc ̇ltekin, S., Akc ̇ltekin, E., Roll, T., Lebius, H. & Schleberger, M. Patterning of insulating surfaces by electronic excitation. *Nucl. Instr. Methods Phys. Res. Sect. B* **267**, 1386-1389 (2009).
40. Karlušić, M. et al. Swift heavy ion track formation in SrTiO_3 and TiO_2 under random, channeling and near-channeling conditions. *J. Phys. D: Appl. Phys.* **50**, 205302 (2017).
41. Karlušić, M. et al. Formation of swift heavy ion tracks on a rutile TiO_2 (001) surface. *J. Appl. Cryst.* **49**, 1704-1712 (2016).
42. Li, W., Wang, L., Lang, M., Trautmann, C. & Ewing, R. C. Thermal annealing mechanisms of latent fission tracks: Apatite vs. zircon. *Earth Planet. Sci. Lett.* **302**, 227-235 (2011).
43. Schattat, B., Bolse, W., Klaum ünzer, S., Zizak, I. & Scholz R. Cylindrical nanopores in NiO induced by swift heavy ions. *Appl. Phys. Lett.* **87**, 173110 (2005).

44. El-Said, A.S. Tracks of 30-MeV C₆₀ clusters in yttrium iron garnet studied by scanning force microscopy. *Nucl. Instrum. Methods Phys. Res., Sect. B* **267**, 953-956 (2009).
45. Ziegler, J. F. & Biersack, J. P. <http://www.srim.org/>
46. Markiewicz, P. & Cynthia Goh, M. Atomic force microscopy probe tip visualization and improvement of images using a simple deconvolution procedure. *Langmuir* **10**, 5-7 (1994).
47. Chase, M. W. Jr. NIST-JANAF Thermochemical Tables. *J. Phys. Chem. Ref. Data Monograph* **9**, 1759 (1998).
48. Hermes, P. et al. Evaporation of atoms from femtosecond laser-heated gallium arsenide. *Appl. Phys. A* **39**, 9-11 (1986).
49. Luo, S. N. et al. Maximum superheating and undercooling: Systematics, molecular dynamics simulations, and dynamic experiments. *Phys. Rev. B* **68**, 134206 (2003).
50. Rethfeld, B., Sokolowski-Tinten, K., Von der Linde, D. & Anisimov, S. I. Ultrafast thermal melting of laser-excited solids by homogeneous nucleation. *Phys. Rev. B* **65**, 092103 (2002).
51. Awazu, K., Fujimaki, M., Ohki, Y. & Komatsubara, T. Photonic crystals of titanium dioxide fabricated by swift heavy ions. *Radiat. Meas.* **40**, 722-729 (2005).
52. Aumayr, F., Facsko, S., El-Said, A. S., Trautmann, C. & Schleberger, M. Single ion induced surface nanostructures: a comparison between slow highly charged and swift heavy ions. *J. Phys.: Condens. Matter* **23**, 393001 (2011).
53. Meftah, A. et al. Swift heavy ions in magnetic insulators: A damage-cross-section velocity effect. *Phys. Rev. B* **48**, 920 (1993).
54. Leino, A. A. et al. Structural analysis of simulated swift heavy ion tracks in quartz. *Nucl. Instrum. Methods Phys. Res., Sect. B* **326**, 289-292 (2014).
55. Afra, B. et al. SAXS investigations of the morphology of swift heavy ion tracks in α -quartz. *J. Phys.: Condens. Matter* **25**, 045006 (2013).
56. Li, W., Lang, M., Gleadow, A. J. W., Zdorovets, M. V. & Ewing, R. C. Thermal annealing of unetched fission tracks in apatite. *Earth Planet. Sci. Lett.* **321-322**,

121-127 (2012).

57. Jensen, J., Dunlop, A., Della-Negra, S. & Pascard, H. Tracks in YIG induced by MeV C₆₀ ions. *Nucl. Instrum. Methods Phys. Res., Sect. B* **135**, 295-301 (1998).

58. Schan, R. et al. New insights on ion track morphology in pyrochlores by aberration corrected scanning transmission electron microscopy. *J. Mater. Res.* **32**, 928-935 (2016).

59. Trachenko, K., Dove, M. T., Artacho, E., Todorov, I. T. & Smith, W. Atomistic simulations of resistance to amorphization by radiation damage. *Phys. Rev. B* **73**, 174207 (2006).

60. Yablinsky, C. A. et al. Characterization of swift heavy ion irradiation damage in ceria. *J. Mater. Res.* **30**, 1473-1484 (2015).

61. Toulemonde, M. et al. Experimental phenomena and thermal spike model description of ion tracks in amorphisable inorganic insulators. *Mat. Fys. Medd.* **52**, 263-292 (2006).

62. Alderman, O. L. G., Skinner, L. B., Benmore, C. J., Tamalonis, A. & Weber, J. K. R. Structure of molten titanium dioxide. *Phys. Rev. B* **90**, 094204 (2014).

63. Touloukian, Y. S. Thermal Conductivity: Non-metallic solids (IFI/Plenum, New York, 1970).

64. Cronemeyer, D. C. Electrical and optical properties of rutile single crystals. *Phys. Rev.* **87**, 876 (1952).

Acknowledgements

This work was financially supported by National Natural Science Foundation of China (Grant Nos. 11405229, 11690041, 41673062 and 11505243). P.Z. acknowledges financial support of CAS "Light of West China" Program. W.L. acknowledges the support of the Thousand Young Talents Program of China. P.Z. and J.L. are grateful to Prof. Marcel Toulemonde for providing the inelastic thermal spike model code generously and some useful discussions. We would like to thank the accelerator staff

of the HIRFL.

Author contributions

P.Z. and J.L. designed experiments, proposed the model and wrote the manuscript. P.Z., W.L. and J.L. provided valuable scientific discussions and improved the manuscript. P.Z., Z.L., P.H. and Y.S. performed the swift heavy ions irradiation experiments. S.N. and L.X. performed TEM characterization. P.Z., J.Z. and S.Z. performed the AFM characterization. P.Z. conducted the i-TS model calculation. All authors discussed the results and approved the final version of the manuscript.

Competing interests: The authors declare no competing interests.

Table 1. Irradiation parameters of rutile (mass density 4.25 g/cm³) for ions with different incident energies. Electronic stopping power (S_e) and ion range (R_p) were calculated with SRIM2013 code⁴⁵. Hillock height (D_h), apparent hillock/track diameter (D_a), corrected hillock diameter (D_c) and yield of track (η) were obtained from the measurements of AFM or TEM.

Ion	Energy (MeV)	Incident angle (°)	S_e (keV/nm)	R_p (μ m)	D_h (nm)	D_a (nm)	D_c (nm)	η
¹²⁹ Xe	860	0	26.9	36.6	4.0 \pm 1.2	18.7 \pm 7.1	4.4 \pm 1.7	0.91
¹²⁹ Xe	1341	45	24.3	55.3	3.1 \pm 0.5	17.1 \pm 2.2	3.7 \pm 1.3	0.83
¹²⁹ Xe	1641	0	22.5	68.1	2.4 \pm 0.6	14.1 \pm 3.0	2.5 \pm 1.3	0.90
¹²⁹ Xe	1940	45	20.9	81.9	2.2 \pm 0.5	13.1 \pm 1.4	2.1 \pm 0.6	0.85
¹²⁹ Xe	2194	45	19.7	94.4	1.8 \pm 0.3	11.3 \pm 1.4	1.6 \pm 0.3	0.92
¹²⁹ Xe	2300	45	19.2	99.9	2.0 \pm 0.4	12.6 \pm 2.6	2.0 \pm 0.8	0.80
¹⁸¹ Ta	829	7	35.1	30.8	7.6 \pm 0.8	25.0 \pm 2.0	7.8 \pm 1.0	0.97
¹⁸¹ Ta	1387	7	33.9	46.9	6.8 \pm 0.9	23.7 \pm 1.5	7.0 \pm 0.8	1.01
¹⁸¹ Ta	1703	7	32.7	56.4	6.2 \pm 1.4	22.5 \pm 1.6	6.3 \pm 1.0	0.97
¹⁸¹ Ta	1786	7	32.4	58.7	6.3 \pm 0.8	22.1 \pm 1.4	6.1 \pm 0.8	1.03
¹⁸¹ Ta	1908	7	32.0	62.7	6.0 \pm 0.8	21.7 \pm 1.4	5.9 \pm 0.8	0.95
²⁰⁹ Bi	894		40.1	29.7		8.6 \pm 1.6		
²⁰⁹ Bi	1390		39.9	42.1		8.4 \pm 1.6		

Table 2. Main physical parameters of rutile TiO₂ for i-TS model calculation.

	TiO ₂
Density (g/cm ³)	4.25 for solid, 3.21 for liquid ⁶²
Specific heat (J/g·K)	0.69 (300 K) - 0.99 (2100 K) ⁴⁷
Thermal conductivity (J/cm·K·s)	0.104 (300 K) - 0.0321 (1400 K) ⁶³
Latent heat of fusion (J/g)	838.07 ⁴⁷
Melting point (K)	2130 ⁴⁷
Energy to melt (eV/at)	0.69 ⁴⁷
Band gap (eV)	3.05 ⁶⁴
Electron-phonon mean free path (nm)	5.8 ^{32-34,36,61}

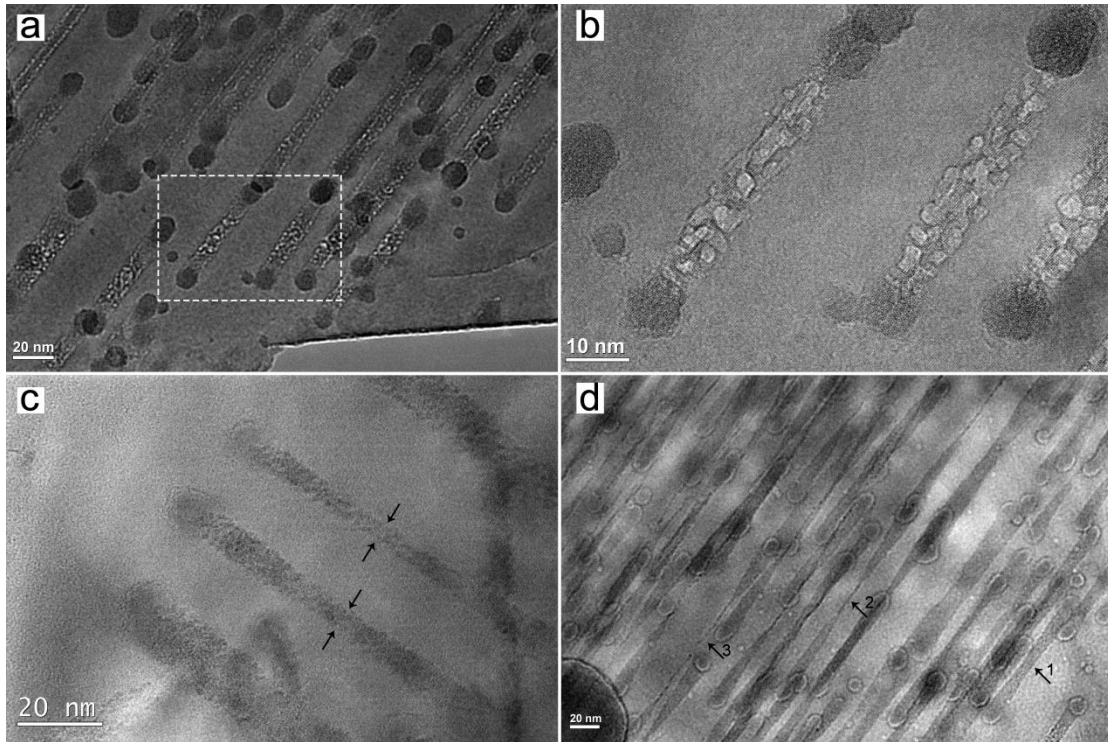


Fig. 1 Bright field TEM micrographs of ion tracks with different morphologies induced by 1390 MeV ^{209}Bi ions in lamella rutile. **a** Ion tracks with nearly cylindrical morphology (underfocused condition). A pair of spherical hillocks at each end of an ion track can be found on both the top and bottom surface when the energetic ions penetrate the entire thickness of a thin sample. **b** HRTEM micrograph from the dotted square in (a) evidently shows that an ion track consists of many irregular shaped voids (underfocused condition). **c** A sandglass-like structure, where the “waist” locations are marked by arrows, is evident when the penetration length in a rutile sample is larger than ~ 60 nm. **d** Sandglass-like tracks with different “waist” diameters, which are strongly correlated with the actual penetration length of an ion in the sample, are marked by arrows.

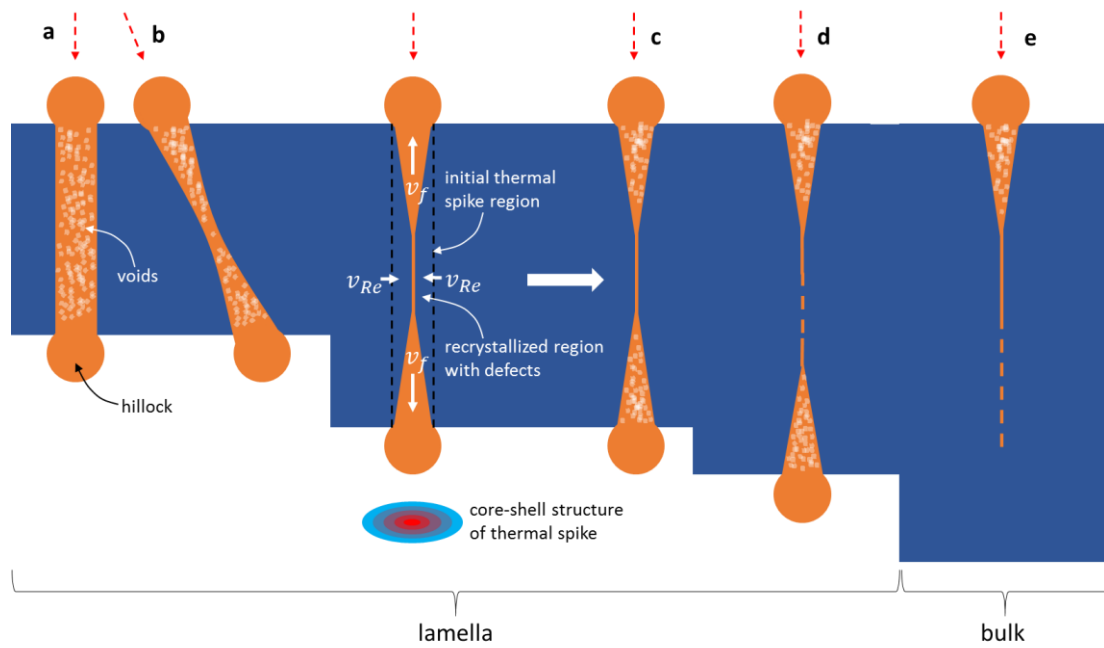


Fig. 2 Diagram for ion track morphology formation as a function of ion path length in rutile. **a** When the ion path length is shorter than about 60 nm, the track morphology is nearly cylindrical. **b** When the ion path length is longer than 60 nm, the sandglass-like morphology emerges. **c** When the ion path length is about 150 nm, two conical features near surface connected with a thin track appears. **d** When the ion path length is longer than 150 nm, the thin track connecting two conical features near surface start to be discontinuous. **e** For the bulk rutile, the conical track appears near the irradiated surface. In the deep, the thin track is discontinuous and finally disappears. In our model, the core-shell structure of thermal spike, fluid velocity v_f and recrystallization velocity v_{Re} contribute to the morphology evolution with the ion path length.

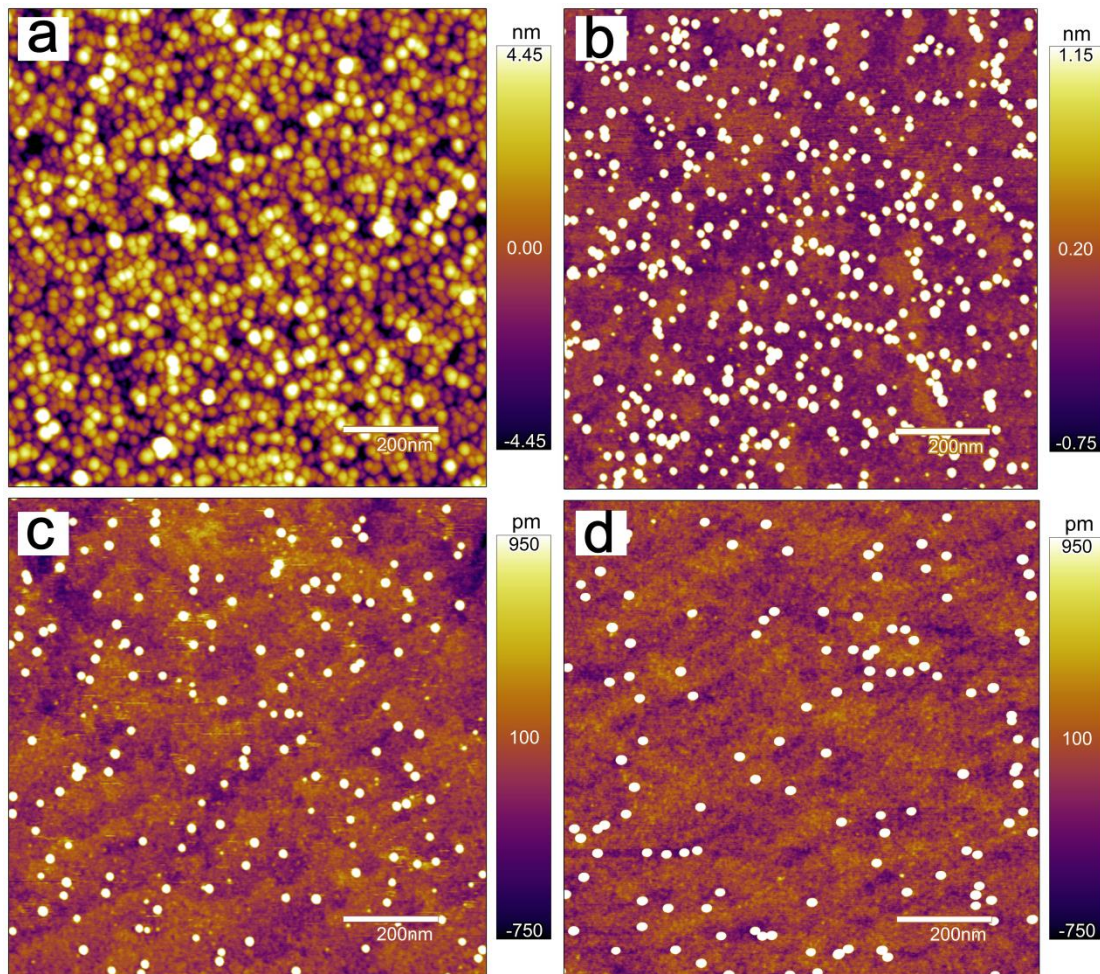


Fig. 3 AFM micrograph of hillocks on the surface of rutile irradiated with swift heavy ions. **a** Hillocks induced by 1390 MeV ^{209}Bi ions ($5 \times 10^{11}/\text{cm}^2$) appear overlapped due to the finite curvature radius of the AFM tip. **b** Hillocks induced by 860 MeV ^{129}Xe ions ($5 \times 10^{10}/\text{cm}^2$). **c** Hillocks induced by 1341 MeV ^{129}Xe ions ($2 \times 10^{10}/\text{cm}^2$). **d** Hillocks induced by 1908 MeV ^{181}Ta ions ($1 \times 10^{10}/\text{cm}^2$). The yield of track is about 80-100%, implying that one ion creates one track.

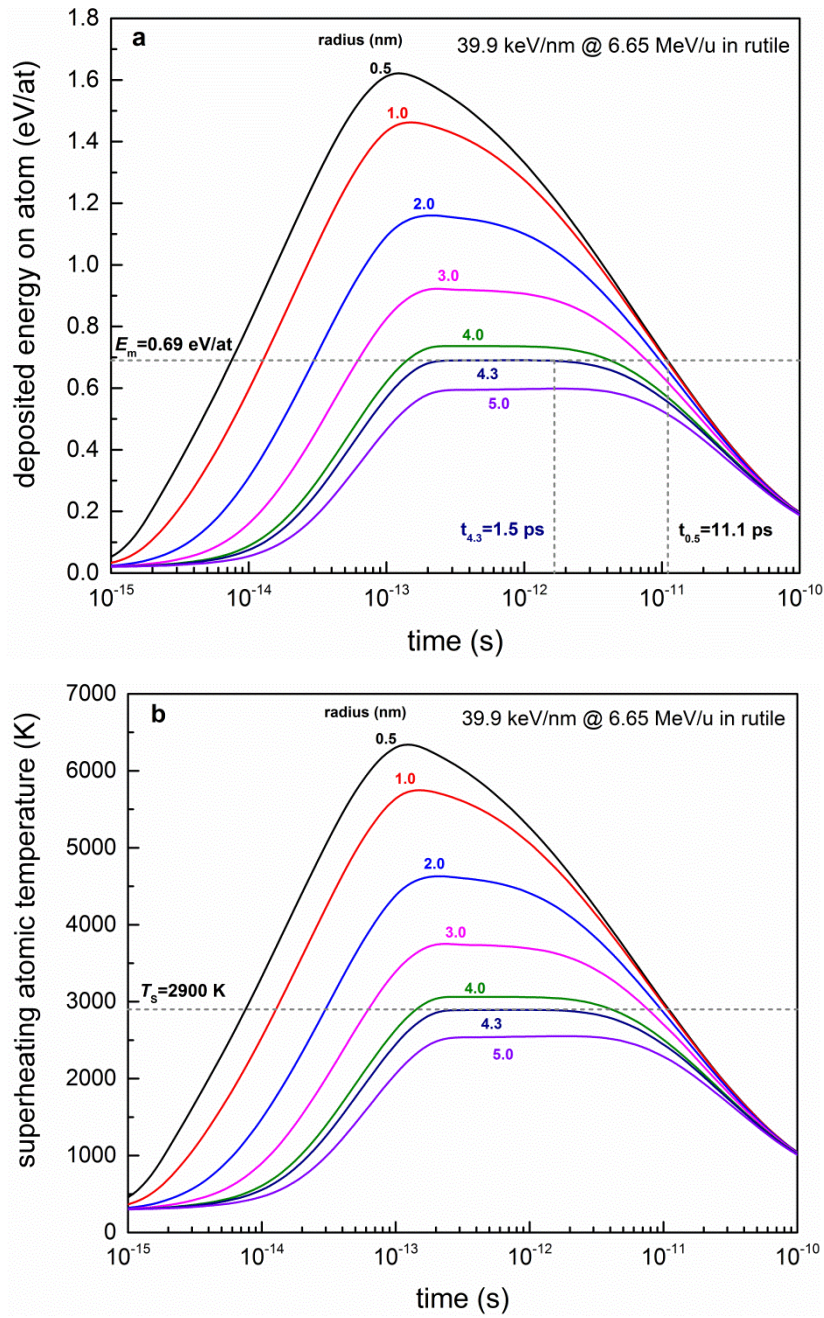


Fig. 4 i-TS calculations for 1390 MeV Bi irradiation in rutile. **a** Deposited energy on atoms versus time. Using the energy to melt E_m 0.69 eV/at⁴⁷, the deduced radius is 4.3 nm. The duration of molten phase for the radius of 0.5 and 4.3 nm are 11.1 and 1.5 ps, respectively. **b** Superheating atomic temperature versus time. For the radius of 4.3 nm, superheating melting temperature is 2900 K.

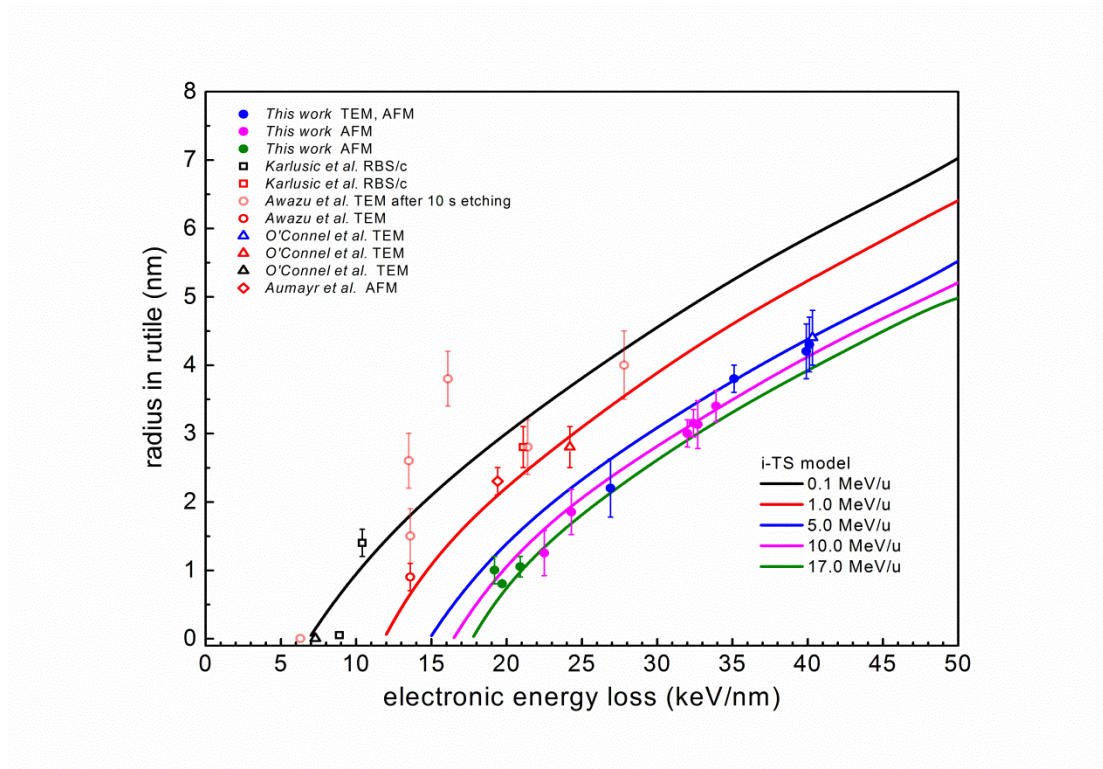


Fig. 5 Experimental radii of ion track in single crystal rutile versus electronic energy loss. The experimental results (with five kinds of colors correspond to different specific energies) are reproduced from Karlusic et al.⁴⁰, Awazu et al.^{36,51}, O'Connell et al.²³, Aumayr et al.⁵² and this work. The solid lines are i-TS calculations for five different specific energies of 0.1, 1.0, 5.0, 10.0 and 17.0 MeV/u, respectively. Note that the data (open circle with pink color) reproduced from Awazu et al.³⁶ are determined by TEM after 20% hydrofluoric acid etching for 10 seconds.

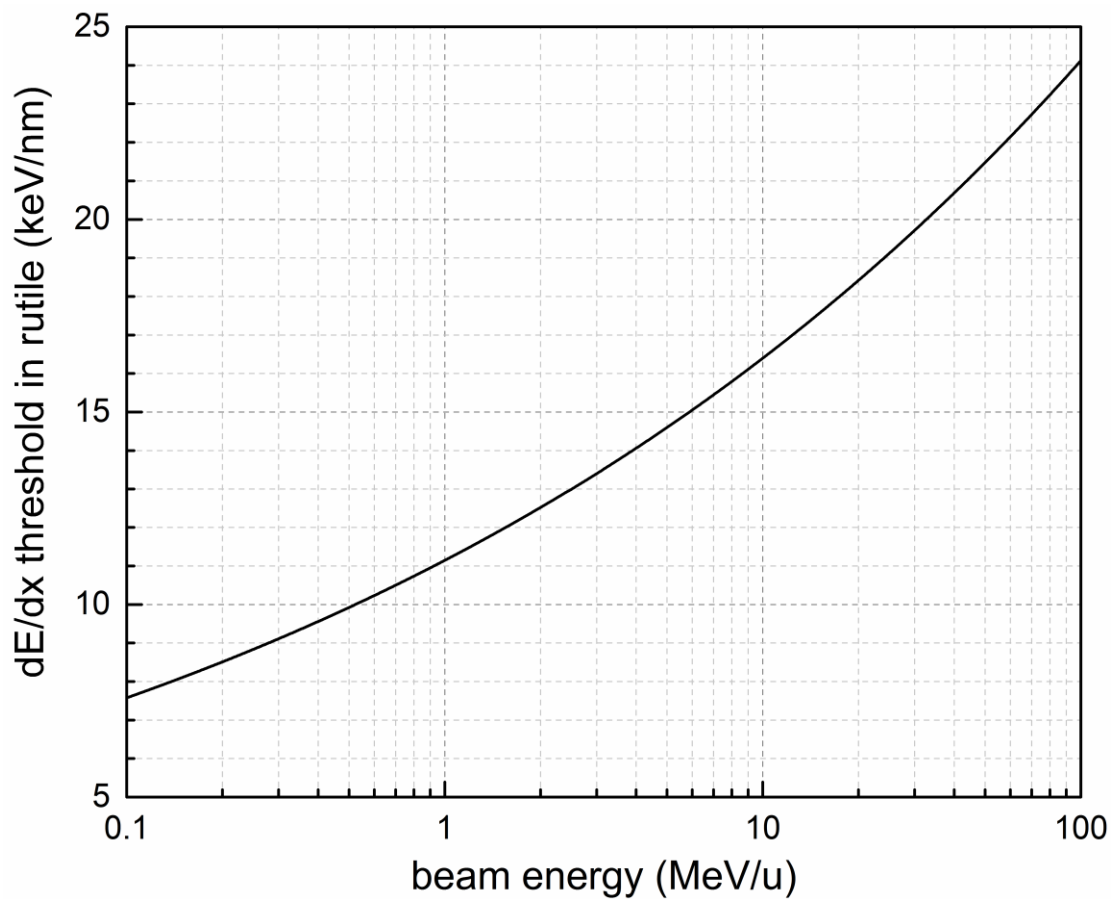


Fig. 6 Threshold of ion track formation in rutile TiO_2 predicted by i-TS model versus beam energy (0.1-100 MeV/u). The threshold ranges from 7 to 24 keV/nm with increasing beam energy, due to the well-established ion velocity effect.